Bidirectional energy cascade in surface capillary waves

L. V. Abdurakhimov,[1,2] M. Arefin,[3] G. V. Kolmakov,[3] A. A. Levchenko,[1] Yu. V. Lvov,[4] and I. A. Remizov[1]

[1]*Institute of Solid State Physics RAS, Chernogolovka, Moscow Region 142432, Russia*

[2]*Okinawa Institute of Science and Technology, Okinawa 904-0495, Japan*

[3]*Physics Department, New York City College of Technology, City University of New York, Brooklyn, New York 11201, USA*

[4]*Department of Mathematical Sciences, Rensselaer Polytechnic Institute, Troy, New York 12180, USA*

(Received 16 April 2014; revised manuscript received 22 December 2014; published 27 February 2015)

Based on an experiment and simulations, we report that an energy cascade in surface capillary waves can be bidirectional, that is, can simultaneously flow towards large and small wavelength scales from the pumping scales. The bidirectional energy cascade provides an effective global coupling mechanism between the scales. We show that formation of the bidirectional cascade leads to creation of large-scale, large-amplitude waves on the fluid surface.

DOI: 10.1103/PhysRevE.91.023021 PACS number(s): 47.27.−i, 68.03.Kn

I. INTRODUCTION

Turbulence in a system of nonlinearly interacting waves is referred to as wave turbulence [1,2]. It is manifested in various physical systems including atmospheric waves [3], Earth's magnetosphere and its coupling with the solar wind [4], interstellar plasmas [5], and ocean wind-driven waves [6]. Surface capillary waves are short waves on a fluid surface, for which surface tension is the primary restoring force. Turbulence of capillary waves is important for the energy and momentum transfer on a fluid surface [1] and for the transfer of gas into solution through a gas-liquid interface [7].

It has been known since the seminal work by Kolmogorov [8] that turbulent dynamics is controlled by a directional energy flux through the wavelength scales. Wave turbulence theory [1,2] based on a kinetic equation for a wave ensemble,

$$\frac{\partial N(\boldsymbol{k})}{\partial t} = \mathrm{St}[N(\boldsymbol{k})], \tag{1}$$

predicts a steady-state, scale-invariant solution that describes a constant flux of energy towards smaller scales. Here $N(\boldsymbol{k})$ is the ensemble-averaged pair correlation function for the wave amplitudes in K representation, $\boldsymbol{k}$ is the wave vector, and $\mathrm{St}[N(\boldsymbol{k})]$ is the statistical "collision" integral, which accounts for the nonlinear wave interactions. The kinetic equation Eq. (1) for waves is similar to the Boltzmann equation for a rarefied gas of particles or quasiparticles [9].

The nonlinear wave system dynamics can be dominated by local or nonlocal interactions between the waves in the frequency scales [1,2]. In the case of local interactions, only waves with comparable wavelength scales interact with each other, whereas for nonlocal interactions the waves split or combine with other waves, which can result in wavelengths significantly different from the initial ones. The locality of the nonlinear interactions is equivalent to the convergence of the collision integral $\mathrm{St}[N(\boldsymbol{k})]$ in the kinetic equation (1) [1,2]. Internal gravity waves in the ocean present an example of a system with nonlocal wave interactions, for which the collision integral diverges in the steady state [10]. For capillary waves, the collision integral converges for a thermodynamic-equilibrium distribution as well as for a steady-state turbulent wave distribution that carries the energy flux through the scales [11]. Thus, capillary wave turbulence is dominated by local interactions and only waves with similar length scales interact with each other. Therefore, the wave energy transfers in a form of a cascade through the scales [11]. For the energy flux directed towards the high-frequency spectral domain, this cascade is referred to as a direct energy cascade. The respective wave spectrum can be viewed as the wave analog of the Kolmogorov spectrum of hydrodynamic turbulence [8,12] and is referred to as the Kolmogorov-Zakharov (KZ) spectrum of wave turbulence [1]. The direct cascade of wave turbulence has been extensively studied in experimental and theoretical works [11,13–19].

In this paper, based on the results of experimental and numerical studies, we report that, in sharp contrast to existing theory and experiments, the energy flux of nonlinear capillary waves can also propagate towards the large-scale, low-frequency spectral region *simultaneously* with a conventional direct cascade. The formation of this bidirectional turbulent cascade results in significant changes in the energy budget of the system. Specifically, small-scale turbulent oscillations are suppressed, whereas sustained high-amplitude large-scale oscillations are formed. A bidirectional cascade of energy was recently predicted for the two-component hydrodynamics in the solar wind [20]. However, such a cascade has never been observed or predicted for capillary waves. Moreover, it has never been observed for systems in which resonant three-wave interactions dominate and no additional integrals of motion are present. We demonstrate that it is the finite viscous damping in the low-frequency domain that results in the bidirectional cascade formation.

Based on our experiment and simulations, the mechanism responsible for formation of the bidirectional energy cascade can be understood as follows. A system of nonlinear waves with no damping at low frequencies establishes a thermodynamical equilibrium spectrum in the low-frequency domain, which carries no energy flux and which temperature is proportional to the pumping rate [21]. However, in experiments with fluids of final depth, low-frequency wave damping occurs due to the viscous drag at the container's walls [22]. The latter results in the decrease of the low-frequency wave amplitudes. The system tends to restore the thermodynamical equilibrium spectrum and, in effect, a steady energy flux towards the low-frequency domain is formed.

We study capillary waves on the surface of superfluid helium (He-II). He-II demonstrates many quantum features, among which are the famous fountain effect in response to heating, extremely high heat conductivity, and quantization of vorticity in the fluid bulk [23]. Nevertheless, oscillations of a free He-II surface behave much like surface oscillations of a classical fluid with very low viscosity [17,23,24]. He-II provides an ideal test bed for studying nonlinear wave dynamics due to the possibility of driving the weakly charged He-II surface directly by an oscillating electric field, virtually excluding the excitation of bulk modes [25]. This method is similar to the oceanographic case where waves are generated due to wind drag applied directly to the fluid surface. Previous experiments with waves on quantum fluids (liquid helium and hydrogen) allowed detailed study of the direct cascade of capillary turbulence [17], including modification of the turbulent spectrum by applied low-frequency driving [26], and the turbulent bottleneck phenomena in the high-frequency spectral domain [24] (see also a comprehensive review in Ref. [27]). In a fluid layer of final depth, vortices can also contribute to the energy transfer to large length scales [28]. In quantum fluids, quantized vortices penetrate to the fluid bulk from the oscillating surface if the amplitude of surface waves is large enough [29]. However, the latter process is only efficient for large dimensionless nonlinearities (i.e., the wave height-to-length ratios) >0.7 [29]. In our experiments with waves on the surface of a quantum fluid, the dimensionless nonlinearity is <0.05 [25] and, thus, in our analysis we disregard the quantized vortex creation.

II. EXPERIMENTAL OBSERVATIONS

A. Steady-state turbulent spectrum

In our experiments helium was condensed into a cylindrical cup formed by a bottom capacitor plate and a guard ring and was positioned in a helium cryostat. The cup has an inner radius of 30 mm and a depth of 4 mm. The experiments were conducted at temperature $T = 1.7$ K of the superfluid liquid. The capillary-to-gravity wave transition on the surface of superfluid helium occurs at a frequency of $\simeq$25 Hz; the respective wavelength is $\lambda = 2\pi(\alpha/\rho g)^{1/2} = 0.17$ cm at $T = 4.2$ K and increases to 0.3 cm for $T = 1.7$ K [27], where α is the surface tension, ρ is the fluid density, and g is the acceleration due to gravity. The finite depth of the waves only influences the linear dispersion relation $\omega = \omega(k)$ at frequencies $\omega/2\pi < 10$ Hz.

The free surface of the liquid was positively charged as a result of β-particle emission from a radioactive plate located in the bulk liquid. Oscillations of the liquid surface were excited by application of an ac voltage $U(t) = U_d \sin(\omega_d t)$ to the upper capacitor plate. Oscillations of the fluid surface elevation $\zeta(\boldsymbol{r},t)$ were detected through variations of the power $P(t)$ of a laser beam reflected from the surface [Fig. 1(a)]. (Here t is time and $\boldsymbol{r}$ is the two-dimensional coordinate in the surface plane.) The capillary wave power spectrum $\zeta(\omega) \propto P(\omega)$ was calculated via the Fourier time transform of the signal $P(t)$ [25]. Figure 1(b) shows a snapshot made through the cryostat glass of turbulent waves on the helium surface. The measurements of wave damping in the cell showed that the quality factor at low frequencies $\omega < \omega_d$ is $Q \sim 10^3$.

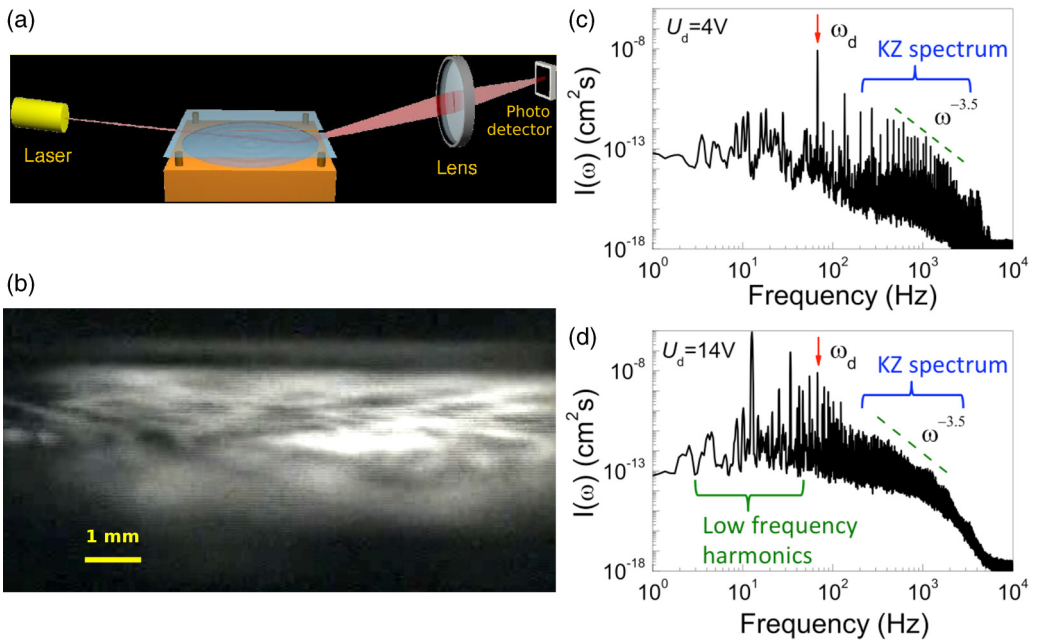

FIG. 1. (Color online) (a) Schematic of the experimental setup. An optical cryostat containing the cell is not shown. (b) Snapshot of the turbulent surface of superfluid helium. The driving frequency is $\omega_d/2\pi = 113$ Hz. (c),(d) Formation of large-amplitude waves on the surface at $\omega < \omega_d$ by increasing the ac driving voltage from $U_d = 4$ V (c) to $U_d = 14$ V (d). The driving frequency (arrow) is $\omega_d/2\pi = 68$ Hz. The wavelength at the driving frequency ω_d is $\simeq$780 μm. The conventional direct Kolmogorov-Zakharov (KZ) spectrum of capillary turbulence $I(\omega) \propto \omega^{-3.5}$ between 2×10^2 Hz $< \omega/2\pi < 2 \times 10^3$ Hz is shown by the dashed line. Formation of low-frequency harmonics at $\omega < \omega_d$ with amplitudes larger than those at the driving frequency ω_d is clearly visible for $U_d = 14$ V.

Figures 1(c) and 1(d) show the evolution of the ensemble-averaged turbulent wave spectrum $I(\omega) = \langle|\xi(\omega)|^2\rangle$ with increasing driving amplitude U_d, when the driving frequency is $\omega_d/2\pi = 68$ Hz. In Fig. 1(c) for a moderate pumping $U_d = 4$ V, the direct KZ cascade forms in the high-frequency domain 2×10^2 Hz $< \omega/2\pi < 2 \times 10^3$ Hz. At very high frequencies $\omega/2\pi \sim 2 \times 10^3$ Hz, the KZ cascade is terminated by bulk viscous damping. Weak low-frequency oscillations at $\omega < \omega_d$, with $I(\omega) \leqslant 10^{-11}$ cm^2 s in Fig 1(c), are caused by mechanical vibrations of the experimental setup.

With an increased driving voltage of $U_d = 14$ V in Fig. 1(d), there are many low-frequency peaks in the spectrum that have heights a few orders of magnitude larger: $I(\omega) \approx 10^{-7}$–$10^{-6}$ cm^2 s. The spectra shown on Figs. 1(c) and 1(d) have pronounced discrete spikes. The spikes are the manifestation of capillary wave turbulence excited by a narrowband driving force, which spectral width is smaller than the characteristic driving frequency; cf. observations for the direct cascade in Refs. [15,30] and simulations in Refs. [31,32].

The total wave energy given by a sum of the energy due to surface tension and the kinetic energy of fluid motion is

$$E = \alpha \int |\nabla\zeta(\boldsymbol{r},t)|^2 d\boldsymbol{r}. \tag{2}$$

Calculations from the data in Fig. 1(d) show that only about 1% of the total wave energy is concentrated in the high-frequency domain $\omega \geqslant \omega_d$, whereas 99% of the energy is localized at frequencies $\omega < \omega_d$.

B. Turbulence buildup

To better understand the turbulence dynamics, we also studied the buildup process of capillary turbulence on the surface of superfluid helium in the presence of low-frequency harmonics. Formation of capillary turbulence after steplike application of a periodic driving force at the moment $t = 0$ is shown in Fig. 2. The surface is driven at the frequency $\omega_d/2\pi = 199$ Hz; the driving amplitude is $U_d = 97$ V. It is seen in Fig. 2(a) that at $t = 1.31$ s after the driving force is turned on, the wave at the driving frequency and its high-frequency harmonics with $\omega/2\pi \leqslant 10^3$ Hz start forming on the noisy background.

At the moment $t = 11.80$ s [Fig. 2(b)] the direct cascade is formed in the frequency range from the driving frequency to the frequency $\sim 2 \times 10^4$ Hz, in agreement with Figs. 1(c) and 1(d) and previous observations [15,27]. However, it is seen in Fig. 2(b) that the wave on the surface with the frequency equal half the driving frequency is also formed by that time. Generation of a wave with $\omega = \omega_d/2$ can be attributed to the modulation instability of the capillary waves due to nonlinearity [33,34].

At the moment $t = 53.74$ s multiple low-frequency harmonics with the frequencies $\omega < \omega_d$ are formed on the wave spectrum, in agreement with with our results for the steady-state measurements [Figs. 1(c) and 1(d)]. From comparison of the spectra in Figs. 2(b) and 2(c) it is evident that the characteristic formation time for the low-frequency harmonics is larger than that for the direct cascade. This observation

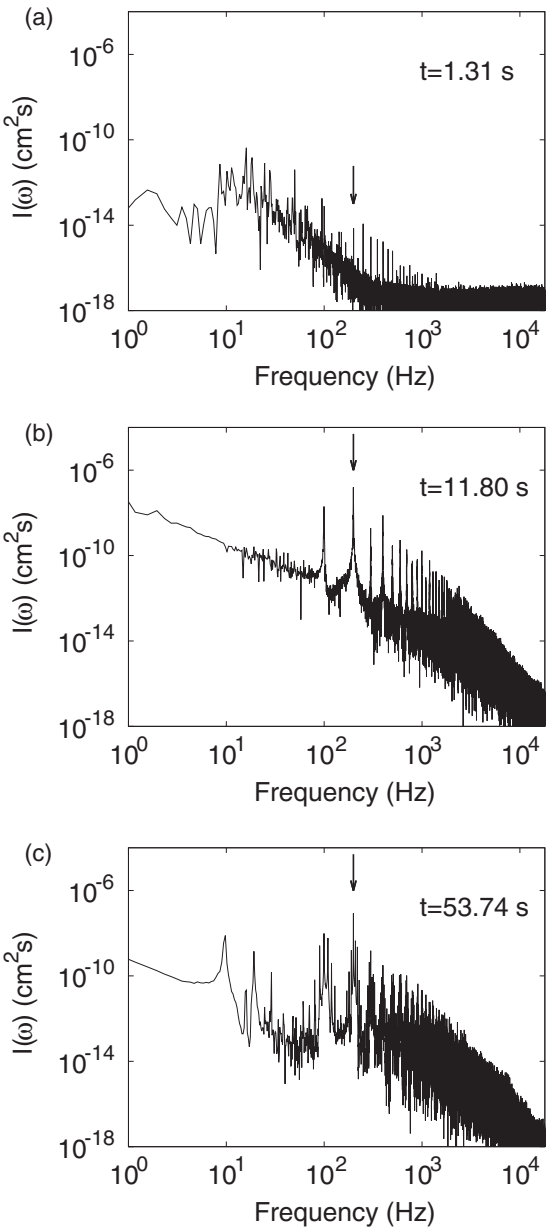

FIG. 2. Buildup of capillary turbulence on the surface of superfluid helium. The spectra are calculated via short-time Fourier transform of the recorded signal. The moments, for which the spectra (a)–(c) are calculated, are labeled on the figure. The driving frequency is $\omega_d/2\pi = 199$ Hz (arrowed) and the driving amplitude is $U_d = 97$ V. Formation of the wave at a frequency equal to half the driving frequency is seen in panel (b), and formation of multiple low-frequency harmonics is seen in (c).

is in qualitative agreement with the observations made for acoustic turbulence of nonlinear second-sound waves in bulk superfluid helium [35]. However, in the case of second sound the wave dispersion relation is close to linear, $\omega \propto k$ [23], and therefore the mechanism of acoustic turbulence is quite different from that for capillary surface waves: formation of correlated shock sound waves rather than strong phase fluctuations for dispersive surface waves [1,35–38].

III. NUMERICAL SIMULATIONS

A. Numerical model

To illustrate the formation of large-amplitude, low-frequency waves, we performed numerical modeling of the wave dynamics in the cylindrical cell with external driving and viscous damping. In the simulations, we assume angular symmetry of the surface. The deviation $\zeta(r,t)$ of the surface from the equilibrium flat state is expressed by time-dependent amplitudes $a_n(t)$ of the normal modes [13],

$$\zeta(r,t) = \sum_n \sqrt{\frac{k_n}{2\omega(k_n)\rho A J_0(\beta_n)^2}}[a_n(t) + a_n^*(t)]J_0(k_n r), \quad (3)$$

where r is the distance from the center of the cell, $J_0(x)$ is the Bessel function of the zero order, $A = \pi R^2$ is the free-surface area, R is the cell radius, $\omega(k) = \sqrt{\alpha k^3/\rho}$ is the linear dispersion relation, $k_n = \beta_n/R$ is the radial wave number, $n > 0$ labels the resonant radial modes, and β_n is the nth zero of the first-order Bessel function $J_1(\beta_n) = 0$. Due to angular isotropy, we utilize the angle-averaged dynamical equation for $a_n(t)$,

$$\begin{aligned}\frac{da_n(t)}{dt} = &-i\sum_{n_1,n_2} V_{n,n_1,n_2} D_{n,n_1,n_2} a_{n_1}(t)a_{n_2}(t)e^{i\Delta\omega_{n,n_1,n_2}t} \\ &- 2i\sum_{n_1,n_2} V^*_{n_1,n,n_2} D_{n_1,n,n_2} a_{n_1}(t)a^*_{n_2}(t)e^{-i\Delta\omega_{n_1,n,n_2}t} \\ &- \gamma(\omega(k_n))a_n(t). \end{aligned} \quad (4)$$

Equations (4) are canonical equations of motion for capillary waves with quadratic nonlinearity and, with an assumption of angular isotropy, are equivalent to the equations of motion of the surface deviation $\zeta(r,t)$ [11].

The coupling coefficients V_{n,n_1,n_2} characterize the interaction strengths between waves with wave numbers k_n, k_{n_1}, and k_{n_2}; instead of taking the exact value for capillary waves, we model it by

$$V_{n,n_1,n_2} = \epsilon\sqrt{\omega(k_n)\omega(k_{n_1})\omega(k_{n_2})}. \quad (5)$$

The coupling coefficients (5) in the model (4) have the same scaling properties with respect to Zakharov's conformal mapping in K space as the respective exact coefficients found from the hydrodynamic equations with the free surface [1]. The asterisk in Eq. (4) denotes complex conjugate, i stands for the imaginary unit, $D_{n,n_1,n_2} = 1/2\pi\,\Delta(k_n,k_{n_1},k_{n_2})$, where $\Delta(k_n,k_{n_1},k_{n_2})$ is the area of the triangle with sides k_n, k_{n_1}, and k_{n_2}, and $\Delta\omega_{n,n_1,n_2} = \omega(k_n) - \omega(k_{n_1}) - \omega(k_{n_2})$ is resonance detuning. In the simulations, $\omega_c = (\rho g^3/\alpha)^{1/4}$ and $\lambda_c = (\alpha/\rho g)^{1/2}$ are used as units of frequency and length, respectively. We consider $n_{\max} = 100$ radial modes. The dimensionless factor $\epsilon \ll 1$ is of the order of the maximum surface slope with respect to the horizontal [13]. We set $\epsilon = 10^{-2}$ as a representative value [25]. Driving was applied by fixing the wave amplitude $a_d \equiv |a_{n_d}(t)|$ at a given value.

To capture the physical effects that remove energy from the system, we add wave damping at both high and low frequencies. Low-frequency damping is the result of viscous drag at the cell bottom [22], and high-frequency damping is caused by bulk viscosity in the fluid [12]. Specifically, we model the wave damping coefficient as

$$\gamma(\omega) = \gamma_{\rm LF}(\omega) + \gamma_{\rm HF}(\omega), \quad (6)$$

which is the sum of damping at low frequencies below the $n_{\rm LF} = 10$ resonance in the cell, with $\gamma_{\rm LF}(\omega) = \gamma_{\rm LF} g_{\rm LF}(\omega)$, as well as damping at high frequencies above the $n_{\rm HF} = 80$ resonance, with $\gamma_{\rm HF}(\omega) = \gamma_{\rm HF} g_{\rm HF}(\omega)$. The range of wave frequencies between the $n_{\rm LF}$ and the $n_{\rm HF}$ can be considered as a "numerical inertial interval" in which damping is absent.

The damping factor at high frequencies was set as $\gamma_{\rm HF} = 5 \times 10^{-2}\omega_c$. Damping at high resonant numbers $n > n_{\rm HF}$ is modeled as $g_{\rm HF}(n) = (n - n_{\rm HF})^2/(n_{\max} - n_{\rm HF})^2$, and $g_{\rm HF}(n) = 0$ for $n \leqslant n_{\rm HF}$. For a fluid layer of finite depth, we model damping at low resonant numbers $n < n_{\rm LF}$ as $g_{\rm LF}(n) = (n_{\rm LF} - n)/n_{\rm LF}$, and $g_{\rm LF}(n) = 0$ for $n \geqslant n_{\rm LF}$. The low-frequency damping coefficient $\gamma_{\rm LF}$ is varied between 0 and $4\gamma_{\rm HF}$.

Under conditions considered in this paper, the three-wave interactions taken into account in Eq. (4) dominate and the four-wave interactions can be neglected, as shown in Sec. III B.

Additionally, the nonlinear frequency broadening of the resonances is much larger than spacing between neighboring resonant frequencies; see Sec. III B. Therefore, the system can be considered as a quasicontinuous one and finite-size mesoscopic effects such as frozen turbulence [11] and resonance clustering [39] do not occur.

To calculate the dependence of $a_n(t)$ on time t, we integrated Eq. (4) until the system reached the steady state. The wave spectrum is calculated as the time-averaged quantity $N(k_n) = \langle|a_n(t)|^2\rangle$. For capillary waves, the time-averaged correlation function is $I(\omega) = N(k(\omega))$, where $N(k)$ is expressed as a function of the wave frequency ω via the relation $k = k(\omega)$ inverse to the linear dispersion relation [25].

B. Quasicontinuous turbulent spectra in a spatially restricted nonlinear wave system

The dynamics of capillary turbulence in a restricted geometry depends on the ratio of the nonlinear resonance broadening and the distance in K space between neighboring resonance frequencies [11,39]. In spatially extended systems where the resonance frequency spectrum is quasicontinuous, these are the three-wave interactions that contribute to the nonlinear wave dynamics of capillary waves [1,2]. In the opposite case of small-size systems where the distance between neighboring resonances is large, the three-wave interactions are out of resonance and, hence, accounting for the next-order, four-wave interactions is of importance [11,39–41]. We emphasize that in both cases, the consideration is limited to weakly nonlinear waves, for which the expansion of the full hydrodynamic equations over the wave amplitude can be applied. In our case, this is guaranteed by the smallness of the maximum surface slope ϵ.

To prove that under our experimental conditions the three-wave interactions are only essential in the dynamical equations (4), we compare the characteristic rates for three-wave and four-wave interaction processes. The rate of the

three-wave interactions is [37,42]

$$\gamma_k^{(3)} = 4\sum_{\mathbf{k}_1,\mathbf{k}_2} |V(k,k_1,k_2)|^2 \,[N(k_1)+N(k_2)]\,\delta_{\mathbf{k}-\mathbf{k}_1-\mathbf{k}_2}\,\mathcal{L}^{(3)}[\omega(k)-\omega(k_1)-\omega(k_2)]$$
$$-4\sum_{\mathbf{k}_1,\mathbf{k}_2} |V(k_1,k_2,k)|^2 \,[N(k_2)-N(k_1)]\,\delta_{\mathbf{k}_1-\mathbf{k}_2-\mathbf{k}}\,\mathcal{L}^{(3)}[\omega(k_1)-\omega(k_2)-\omega(k)]$$
$$-4\sum_{\mathbf{k}_1,\mathbf{k}_2} |V(k_2,k,k_1)|^2 \,[N(k_1)-N(k_2)]\,\delta_{\mathbf{k}_2-\mathbf{k}-\mathbf{k}_1}\,\mathcal{L}^{(3)}[\omega(k_2)-\omega(k)-\omega(k_1)], \tag{7}$$

where $N(k_n)$ is the ensemble-averaged pair correlation function for the wave amplitudes of the mode with the resonance number n, the factor

$$\mathcal{L}^{(3)}(\Delta\omega) = \frac{\Gamma_{k12}}{(\Delta\omega)^2+\Gamma_{k12}^2} \tag{8}$$

accounts for nonlinear and viscous broadening of the resonances, and

$$\Gamma_{k12} = \gamma_k + \gamma_{k_1} + \gamma_{k_2} \tag{9}$$

is the total resonance width. The total resonance width is estimated in Eq. (9) as a sum of individual broadenings of the resonances [37,42]. In Eq. (7), the coupling coefficients for the three-wave interactions are expressed as functions of the wave vectors; thus, $V(k_{n_1},k_{n_2},k_{n_3}) \equiv V_{n_1,n_2,n_3}$, where V_{n_1,n_2,n_3} were introduced in Sec. III A. We consider an isotropic case where the correlation functions n_k do not depend on the direction of the wave vector k. Isotropic turbulence is usually considered as a general case in the wave turbulence theory in the absence of the linear momentum flux along the surface [1]. Additionally, the angular symmetry is dictated in our experiment by the cylindrical geometry of the cell. For angular symmetry, Eq. (7) reads after averaging over the directions of the wave vectors $\boldsymbol{k}$, $\boldsymbol{k}_1$, and $\boldsymbol{k}_2$,

$$\gamma_k^{(3)} = 4\sum_{k_1,k_2} \frac{k_1k_2|V(k,k_1,k_2)|^2}{2\pi\,\Delta(k,k_1,k_2)}\,[N(k_1)+N(k_2)]\,\mathcal{L}^{(3)}[\omega(k)-\omega(k_1)-\omega(k_2)]$$
$$-4\sum_{k_1,k_2} \frac{k_1k_2|V(k_1,k_2,k)|^2}{2\pi\,\Delta(k,k_1,k_2)}\,[N(k_2)-N(k_1)]\mathcal{L}^{(3)}[\omega(k_1)-\omega(k_2)-\omega(k)]$$
$$-4\sum_{k_1,k_2} \frac{k_1k_2\,|V(k_2,k,k_1)|^2}{2\pi\,\Delta(k,k_1,k_2)}[N(k_1)-N(k_2)]\mathcal{L}^{(3)}[\omega(k_2)-\omega(k)-\omega(k_1)], \tag{10}$$

where summation in Eq. (10) is made over the absolute values of the vectors. In Eq. (10) we use the following identity for the angle-averaged Dirac δ [1],

$$\frac{1}{(2\pi)^3}\int_0^{2\pi} d\theta_1 \int_0^{2\pi} d\theta_2 \int_0^{2\pi} d\theta_3\,\delta_{\mathbf{k}_1-\mathbf{k}_2-\mathbf{k}_3} = \frac{1}{2\pi\,\Delta(k_1,k_2,k_3)}, \tag{11}$$

where θ_1, θ_2, and θ_3 are the directions of the vectors $\mathbf{k}_1$, $\mathbf{k}_2$, and $\mathbf{k}_3$, respectively.

The rate of the four-wave interactions is

$$\gamma_k^{(4)} = \sum_{\mathbf{k}_1,\mathbf{k}_2,\mathbf{k}_3} |T(k,k_1,k_2,k_3)|^2\,[N(k_1)N(k_3)+N(k_1)N(k_2)-N(k_2)N(k_3)]\delta_{\mathbf{k}+\mathbf{k}_1-\mathbf{k}_2-\mathbf{k}_3}\mathcal{L}^{(4)}[\omega(k)+\omega(k_1)-\omega(k_2)-\omega(k_3)], \tag{12}$$

where the coupling coefficients $T(k,k_1,k_2,k_3)$ characterize the four-wave interactions for waves with the wave vectors $\boldsymbol{k}$, $\boldsymbol{k}_1$, $\boldsymbol{k}_2$, and $\boldsymbol{k}_3$. Following the same approximation as in Sec. III A, we model it as follows:

$$T(k,k_1,k_2,k_3) = \epsilon^2\sqrt{\omega(k)\omega(k_1)\omega(k_2)\omega(k_3)}. \tag{13}$$

The model (13) has the same scaling properties as the exact coupling coefficients [1]. After averaging over the directions of the wave vectors $\mathbf{k}$, $\mathbf{k}_1$, $\mathbf{k}_2$, and $\mathbf{k}_3$, one obtains

$$\gamma_k^{(4)} = \sum_{k_1,k_2,k_3} k_1k_2k_3|T(k,k_1,k_2,k_3)|^2\,[N(k_1)N(k_3)+N(k_1)N(k_2)-N(k_2)N(k_3)]\frac{16\pi}{kk_1+k_2k_3}F\left(\frac{2\sqrt{kk_1k_2k_3}}{kk_1+k_2k_3}\right)$$
$$\times\mathcal{L}^{(4)}[\omega(k)+\omega(k_1)-\omega(k_2)-\omega(k_3)]. \tag{14}$$

Dirac δ in Eq. (14) is averaged as [43]

$$\frac{1}{(2\pi)^4}\int_0^{2\pi} d\theta \int_0^{2\pi} d\theta_1 \int_0^{2\pi} d\theta_2 \int_0^{2\pi} d\theta_3\,\delta_{\mathbf{k}+\mathbf{k}_1-\mathbf{k}_2-\mathbf{k}_3} = \frac{16\pi}{kk_1+k_2k_3}F\left(\frac{2\sqrt{kk_1k_2k_3}}{kk_1+k_2k_3}\right), \tag{15}$$

where $F(x)$ is a complete elliptic integral of the first kind. We denote in Eq. (14)

$$\mathcal{L}^{(4)}(\Delta\omega) = \frac{\Gamma_{k123}}{(\Delta\omega)^2 + \Gamma_{k123}^2} \tag{16}$$

and

$$\Gamma_{k123} = \gamma_k + \gamma_{k_1} + \gamma_{k_2} + \gamma_{k_3}. \tag{17}$$

The angle averaged sums in Eqs. (10) and (14) are numerically indistinguishable from the discrete sums in (7) and (12), respectively, everywhere except a few lowest wave numbers. We set in Eqs. (9) and (17) the total width of the resonances as

$$\gamma_k = \gamma_k^{(3)} + \gamma_k^{(4)} + \gamma_k^{(\mathrm{visc})}, \tag{18}$$

where $\gamma_k^{(\mathrm{visc})}$ is linear viscous broadening of a resonance with the wave number k. We model viscous broadening as $\gamma_k^{(\mathrm{visc})} = \omega(k)/Q$, where Q is the quality Q factor. We set $Q = 10^3$ in agreement with our experimental parameters. Estimation of the total resonance width in Eq. (18) as a sum of broadenings arising from different incoherent processes is a widely used approximation [44].

To find the three- and four-wave interaction rates, $\gamma_k^{(3)}$ and $\gamma_k^{(4)}$, we solved Eqs. (10), (12), and (18) self-consistently. For that purpose we used an iterative procedure. The initial width of the resonances for the iterative procedure has been set equal to their viscous width $\gamma_k^{(\mathrm{visc})}$. We found that the three- and four-wave interaction rates, to which the results of the iterative procedure converge, only weakly depend on Q. It is because in turbulence one has $\gamma_k \gg \gamma_k^{(\mathrm{visc})}$ [1]. We focused on the wave-turbulent regime and therefore, we set the occupation numbers in Eqs. (10) and (12) in the known scale-invariant form [1]

$$N(k) = Ck^{-\frac{17}{4}}. \tag{19}$$

In our simulations, we set $C = 1$. We found that the procedure converges with the relative accuracy $\leqslant 0.2\%$ after ten subsequent iterations.

The obtained dependencies of $\gamma_k^{(3)}$ and $\gamma_k^{(4)}$ on the resonance number n are shown in Fig. 3. We remind that n labels the wave number k of the radial resonant mode. The calculations were done for the cell radius $R = 30\lambda_c$. It is seen in Fig. 3 that the three-wave interaction rate $\gamma_k^{(3)}$ is about an order larger than the four-wave interaction rate $\gamma_k^{(4)}$ for *all wave vectors*. In other words, the characteristic time for the three-wave interaction processes, $\tau_k^{(3)} = 1/\gamma_k^{(3)}$ is much shorter than that for four-wave interaction processes $\tau_k^{(4)} = 1/\gamma_k^{(4)}$ in the whole range of wave vectors. Therefore, the contribution of the four-wave interactions to the capillary wave dynamics is negligible under the conditions described in the paper. It also follows from Fig. 3 that the three-wave interaction rate $\gamma_k^{(3)}$ is larger than the spacing between two neighboring resonances $\Delta\omega_k$. Thus, the resonances overlap within their nonlinear widths and, in effect, the system can be considered as a quasicontinuous one [11,41].

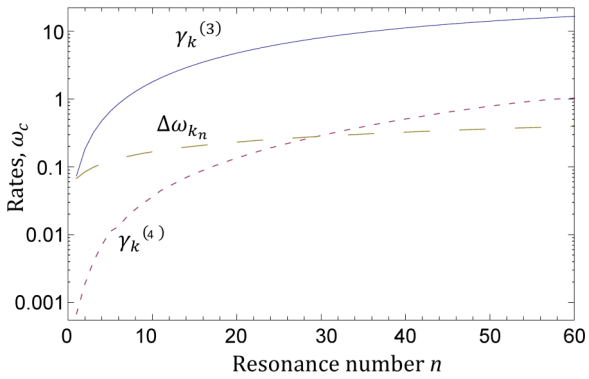

FIG. 3. (Color online) Three- and four-wave interaction rates, $\gamma_k^{(3)}$ (solid curve) and $\gamma_k^{(4)}$ (short-dashed curve) calculated from Eqs. (10), (12), and (18) as functions of the resonance number n. It is seen that one has $\gamma_k^{(3)} \gg \gamma_k^{(4)}$ for all resonance numbers n; thus, the three-wave processes dominate. For comparison, the distance between two neighboring resonances $\Delta\omega_{k_n} \equiv \omega(k_{n+1}) - \omega(k_n)$ is also shown by a long-dashed curve. The discreteness of the resonance frequency spectrum is inessential since $\gamma_k^{(3)} > \Delta\omega_{k_n}$.

C. Bidirectional energy cascade of capillary turbulence

The results of our simulations are summarized in Fig. 4. In Fig. 4(a) (pulses) the steady-state wave spectrum $I(\omega)$ is similar to that observed in the experiment for high-amplitude driving $U_d = 14$ V [cf. Fig. 1(d)]. In the domain $\omega > \omega_d$, the high-frequency KZ spectrum forms in agreement with current and previous observations. We emphasize that, in both the experiment and simulations, the low-frequency waves with $\omega < \omega_d$ retain finite values; moreover, the amplitudes of some low-frequency waves exceed those at the driving frequency ω_d. The fluctuations of the wave amplitudes in Fig. 4(a) (pulses) are probably caused by the effect of the narrowband pumping for the low-frequency harmonics, that is, by the same effect that results in the high-frequency wave amplitude fluctuations in the direct cascade; cf. Sec. II A above and Refs. [15,30–32].

To explain the formation of the low-frequency waves, we demonstrate that bidirectional energy flux is established in the system in place of the traditional direct energy cascade. In the simulations, we varied the low-frequency damping and kept all other parameters fixed. We analyze the energy balance in the system in the form of the continuity equation for energy [1,12],

$$\frac{dE(\omega)}{dt} + \Pi = -\Gamma(\omega) + S(\omega), \tag{20}$$

where $E(\omega) = \int_0^\omega \varepsilon(\omega')d\omega'$ is the total wave energy in the spectral domain $\omega' < \omega$, $\varepsilon(\omega) = 2\pi\alpha k(\omega) \times [dk(\omega)/d\omega]\omega I(\omega)$ is the spectral energy density, Π is the total energy flux, $\Gamma(\omega) = 2\int_0^\omega \gamma(\omega')\varepsilon(\omega')d\omega'$ is the energy loss due to viscous damping, and $S(\omega)$ is the energy source from the driving. In the steady state $dE(\omega)/dt = 0$, the total energy balance in the low-frequency spectral domain $\omega < \omega_d$ is

$$\Pi = -4\pi\alpha \int_0^\omega \gamma(\omega')k(\omega')\left[\frac{dk(\omega')}{d\omega'}\right]\omega' I(\omega')d\omega', \tag{21}$$

because the source term is $S(\omega)$ is absent for low frequencies. To investigate the dependence of the energy flux on the system parameters, we calculated Π from Eq. (21) for different

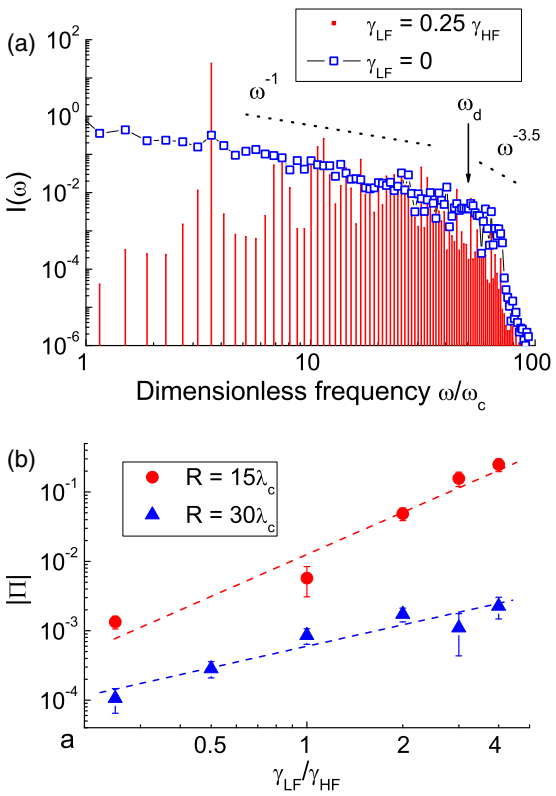

FIG. 4. (Color online) (a) Numerical steady-state spectrum $I(\omega)$ of sustained surface oscillations in the presence of low- and high-frequency damping (peaks) and in the presence of only high-frequency damping (open squares). The spectra are shown in units of $\lambda_c^2\omega_c^{-1}$. The spectra are averaged over an interval of $10^6 t_c$, where $t_c = \omega_c^{-1}$ is a numerical unit of time. The surface is driven at a frequency ω_d of the 50th resonance (arrowed). The power-law spectral behavior $I(\omega) \propto \omega^{-3.5}$ (KZ) and ω^{-1} (the thermal equilibrium) are shown by dashed lines. The radius of the cylindrical cell is $R = 15\lambda_c$. (b) Absolute value of the energy flux, $|\Pi|$, in units of $\alpha\omega_c$, incoming to the spectral domain $\omega < \omega_d$ as a function of the low-frequency damping coefficient γ_{LF}. The cell radii are $R = 15\lambda_c$ (circles) and $30\lambda_c$ (triangles). Vertical bars show the fluctuations of the flux as a standard deviation about the mean. The dashed lines are shown to guide the eye.

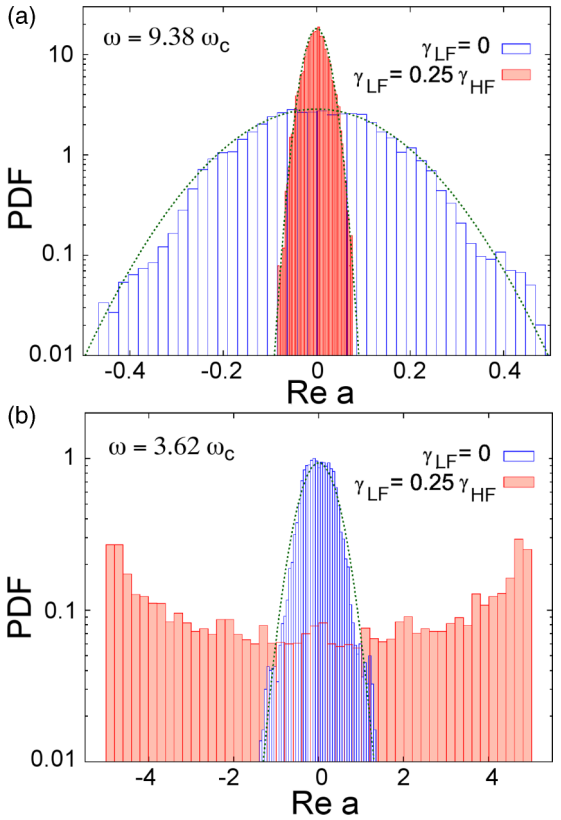

FIG. 5. (Color online) Probability distribution functions of Re(a) for the 20th resonant mode at frequency $\omega = 9.38\omega_c$ (a) and for the 10th mode at frequency $\omega = 3.62\omega_c$ (b) in the absence of low-frequency damping, $\gamma_{LF} = 0$ (open columns), and at $\gamma_{LF} = 0.25\gamma_{HF}$ (shaded columns). PDFs are calculated for the spectra shown in Fig. 4(a). Dashed (green) lines show the Gaussian fit to the PDFs. The line segments connecting the points are shown to guide the eye.

low-frequency damping coefficients and two cell radii [see Fig. 4(b)]. In the absence of low-frequency damping, $\gamma_{LF} = 0$, the thermodynamic-equilibrium Rayleigh-Jeans-like spectrum $I(\omega) \propto \omega^{-1}$ is formed at $\omega < \omega_d$ [Fig. 4(a), open squares], in agreement with Ref. [21]. This spectrum produces no energy flux through the frequency scales. The absolute value of the flux increases with the rise of the low-frequency damping coefficient, as is seen in Fig. 4(b). The negative sign of Π for finite low-frequency dampings in Eq. (21) corresponds to the flux direction from the driving scales, $\omega \sim \omega_d$, towards the low-frequency domain.

We emphasize that in both cases $R = 15\lambda_c$ and $30\lambda_c$, the wave system is driven at the frequency of the 50th resonance. Since the wave frequency at a given resonance number decreases with the rise of the cell radius (cf. Sec. III A), the driving frequency for $R = 30\lambda_c$ [triangles in Fig. 4(b)] is lower than that for $R = 15\lambda_c$ (circles). Therefore, from Fig. 4(b) it follows that the effect of the bidirectional cascade is more pronounced in the case of the high-frequency driving.

D. Probability distribution functions

Wave turbulence predicts that the probability distribution function (PDF) for wave amplitudes with specified wave numbers is a Gaussian function. We verified numerically that this is indeed the case for most modes. Specifically, we calculated a real part of the complex wave amplitude, $Re(a_n)$, as shown in Fig. 5(a). The real part of the amplitudes corresponds to the normalized surface elevation of the surface above a flat equilibrium state, as follows from Eq. (3).

However, some modes showed significant deviations from the predicted Gaussian form when low-frequency damping is applied, as shown by the 10th mode in Fig. 5(b). The non-Gaussian tails in the PDF in the presence of the bidirectional energy cascade correspond to an increased probability of the resonant formation of large-amplitude waves, which may be thought of as a capillary-wave analog of "rogue" waves observed in the ocean [45]. Rogue capillary waves on water surface were recently observed under parametric excitation conditions in Ref. [18].

It is worth noting that for $\gamma_{\rm LF} = 0$ [Fig. 4(a), open squares], the ratio of the spectral powers at $\omega = 3.62\omega_c$ and $9.38\omega_c$ is $\approx$5. Since in this case PDF for the wave amplitudes is close to Gaussian, it is natural to expect that the ratio of PDF widths for the respective amplitudes in Fig. 5 for the two frequencies is $\sim\sqrt{5} \approx 2.2$. It is seen in Fig. 5 that this is indeed the case. However, for $\gamma_{\rm LF} > 0$, PDF for $\omega = 3.62\omega_c$ strongly deviates from the Gaussian form [Fig. 5(b), shaded bars] and thus, such simple estimate for the distribution widths is not valid.

IV. CONCLUSIONS

In conclusion, we demonstrated that energy flux from the driving scale towards the damping region can be formed for capillary waves even if the damping occurs at frequencies lower than the driving frequency. This bidirectional energy flux provides a continuous energy source for sustained low-frequency wave oscillations in the presence of finite damping. Furthermore, bidirectional energy flux provides an effective global coupling mechanism between the scales. In our experiments, we studied nonlinear capillary waves on the surface of superfluid He-II. However, the concept of bidirectional energy flux is relevant for a wider range of nonlinear systems, such as waves on classical fluids in wave tanks [46] and in restricted geometries [47], vibrating elastic plates [48], and quantum fluids [35].

ACKNOWLEDGMENTS

The authors are grateful to L. P. Mezhov-Deglin and W. L. Siegmann for valuable discussions. M.A. and G.V.K. gratefully acknowledge support from the Professional Staff Congress – City University of New York Award No. 66140-0044. M.A. and G.V.K. are also grateful to Army Research Office, Grant #64775-PH-REP, for partial support. The work of M.A. was supported in part by the Emerging Scholars Program at New York City College of Technology of the City University of New York. Yu.V.L. is grateful for support to the Office of Naval Research, Award No. N000141210280. L.V.A., A.A.L., and I.A.R. are grateful to the Russian Science Foundation, Grant No. 14-22-00259. The authors are grateful to the Center for Theoretical Physics at New York City College of Technology of the City University of New York for providing computational resources.

[1] V. E. Zakharov, V. S. L'vov, and G. Falkovich, *Kolmogorov Spectra of Turbulence I* (Springer, Berlin, 1992).
[2] S. Nazarenko, *Wave Turbulence* (Springer-Verlag, Heidelberg, 2011).
[3] L. M. Smith and Y. Lee, J. Fluid Mech. **535**, 111 (2005).
[4] D. J. Southwood, Nature (London) **271**, 309 (1978).
[5] G. S. Bisnovatyi-Kogan and S. A. Silich, Rev. Mod. Phys. **67**, 661 (1995).
[6] Y. Toba, J. Ocean. Soc. Jpn. **29**, 209 (1973).
[7] A. J. Szeri, J. Fluid Mech. **332**, 341 (1997).
[8] A. N. Kolmogorov, Dokl. Akad. Nauk SSSR **30**, 299 (1941).
[9] E. M. Lifshitz and L. P. Pitaevskii, *Physical Kinetics* (Pergamon, Oxford, UK, 1981).
[10] Y. V. Lvov and E. G. Tabak, Phys. Rev. Lett. **87**, 168501 (2001).
[11] A. N. Pushkarev and V. E. Zakharov, Phys. D **135**, 98 (2000).
[12] U. Frisch, *Turbulence* (Cambridge University Press, Cambridge, UK, 1995).
[13] V. E. Zakharov and N. N. Filonenko, J. Appl. Mech. Tech. Phys. **8**, 37 (1967).
[14] W. B. Wright, R. Budakian, D. J. Pine, and S. J. Putterman, Science **278**, 1609 (1997).
[15] E. Henry, P. Alstrom, and M. T. Levinsen, Europhys. Lett. **52**, 27 (2000).
[16] E. Falcon, C. Laroche, and S. Fauve, Phys. Rev. Lett. **98**, 094503 (2007).
[17] L. V. Abdurakhimov, M. Y. Brazhnikov, and A. A. Levchenko, Low Temp. Phys. **35**, 95 (2009).
[18] M. Shats, H. Punzmann, and H. Xia, Phys. Rev. Lett. **104**, 104503 (2010).
[19] L. Deike, M. Berhanu, and E. Falcon, Phys. Rev. E **89**, 023003 (2014).
[20] H. Che, M. L. Goldstein, and A. F. Viñas, Phys. Rev. Lett. **112**, 061101 (2014).
[21] E. Balkovsky, G. Falkovich, V. Lebedev, and I. Y. Shapiro, Phys. Rev. E **52**, 4537 (1995).
[22] B. Christiansen, P. Alstrom, and M. T. Levinsen, J. Fluid Mech. **291**, 323 (1995).
[23] I. M. Khalatnikov, *An Introduction to the Theory of Superfluidity* (Benjamin, New York, 1965).
[24] L. V. Abdurakhimov, M. Y. Brazhnikov, I. A. Remizov, and A. A. Levchenko, JETP Lett. **91**, 271 (2010).
[25] M. Brazhnikov, A. Levchenko, and L. Mezhov-Deglin, Instrum. Exp. Tech. **45**, 758 (2002).
[26] M. Y. Brazhnikov, G. V. Kolmakov, A. A. Levchenko, and L. P. Mezhov-Deglin, JETP Lett. **82**, 565 (2005).
[27] G. V. Kolmakov, M. Y. Brazhnikov, A. A. Levchenko, A. V. Abdurakhimov, P. V. E. McClintock, and L. P. Mezhov-Deglin, in *Progress in Low Temperature Physics: Quantum Turbulence*, edited by W. P. Halperin and M. Tsubota (Elsevier, Amsterdam, 2009), Vol. 16, pp. 303–349.
[28] H. Xia, D. Byrne, G. Falkovich, and M. Shats, Nat. Phys. **7**, 321 (2011).
[29] D. Kobyakov, V. Bychkov, E. Lundh, A. Bezett, and M. Marklund, Phys. Rev. A **86**, 023614 (2012).
[30] M. Y. Brazhnikov, G. V. Kolmakov, and A. A. Levchenko, J. Exp. Theor. Phys. **95**, 447 (2002).
[31] G. E. Fal'kovich and A. V. Shafarenko, Sov. Phys. JETP **68**, 1393 (1988).
[32] M. Y. Brazhnikov, G. V. Kolmakov, A. A. Levchenko, L. P. Mezhov-Deglin, and P. V. E. McClintock, J. Low Temp. Phys. **139**, 523 (2005).
[33] A. I. Dyachenko and V. E. Zakharov, JETP Lett. **81**, 255 (2005).
[34] M. Onorato, A. R. Osborne, M. Serio, and S. Bertone, Phys. Rev. Lett. **86**, 5831 (2001).
[35] A. N. Ganshin, V. B. Efimov, G. V. Kolmakov, L. P. Mezhov-Deglin, and P. V. E. McClintock, Phys. Rev. Lett. **101**, 065303 (2008).

[36] H. Davidowitz, Y. Lvov, and V. Steinberg, Phys. D **84**, 635 (1995).
[37] V. S. L'vov, Y. L'vov, A. C. Newell, and V. Zakharov, Phys. Rev. E **56**, 390 (1997).
[38] G. V. Kolmakov, V. B. Efimov, A. N. Ganshin, P. V. E. McClintock, and L. P. Mezhov-Deglin, Phys. Rev. Lett. **97**, 155301 (2006).
[39] E. Kartashova, *Nonlinear Resonance Analysis* (Cambridge University Press, Cambridge, UK, 2010).
[40] A. N. Pushkarev and V. E. Zakharov, Phys. Rev. Lett. **76**, 3320 (1996).
[41] V. S. L'vov and S. Nazarenko, Phys. Rev. E **82**, 056322 (2010).
[42] Y. V. Lvov, K. L. Polzin, and N. Yokoyama, J. Phys. Oceanogr. **42**, 669 (2011).
[43] S. Dyachenko, A. Pushkarev, and V. E. Zakharov, Phys. D **57**, 96 (1992).
[44] I. I. Sobelman, L. A. Vainshtein, and E. A. Yukov, *Excitation of Atoms and Broadening of Spectral Lines*, Springer Series in Chemical Physics (Springer-Verlag, New York, 1981), Vol. 7.
[45] R. G. Dean, in *Water Wave Kinetics*, edited by A. Torum and O. T. Gudmestad (Kluwer, Amsterdam, 1990), pp. 609–612.
[46] S. Lukaschuk, S. Nazarenko, S. McLelland, and P. Denissenko, Phys. Rev. Lett. **103**, 044501 (2009).
[47] E. Herbert, N. Mordant, and E. Falcon, Phys. Rev. Lett. **105**, 144502 (2010).
[48] B. Miquel, A. Alexakis, C. Josserand, and N. Mordant, Phys. Rev. Lett. **111**, 054302 (2013).